applied sciences

MDPI

Article

In Silico Investigation of an Innovative Cone-Beam CT Configuration for Quantitative Imaging

Antonio Sarno [1,2], Ivan Veronese [1,2,*], Paolo Mauriello [3], Immacolata Vanore [3], Antonio Minopoli [3], Carlos Maximiliano Mollo [4], Silvio Pardi [4], Gianfranco Paternò [5], Mariagabriella Pugliese [3,4], Riccardo de Asmundis [4] and Paolo Cardarelli [5]

[1] Dipartimento di Fisica "Aldo Pontemoli", Università degli Studi di Milano, via Celoria 16, 20133 Milano, Italy; antonio.sarno@unimi.it
[2] INFN Sezione di Milano, via Celoria 16, 20133 Milano, Italy
[3] Dipartimento di Fisica "Ettore Pancini", Università di Napoli Federico II, Compl. Univ. MSA via Cinthia 21, 80126 Napoli, Italy; antonio.minopoli@unicatt.it (A.M.)
[4] INFN Sezione di Napoli, Compl. Univ. MSA via Cinthia 21, 80126 Napoli, Italy
[5] INFN Sezione di Ferrara, via G. Saragat 1, 44122 Ferrara, Italy
* Correspondence: ivan.veronese@unimi.it

Abstract

Quantitative evaluations in 3D images acquired via Cone-Beam Computed Tomography (CBCT) are limited by the scatter abundance and cone-beam artifacts. This work investigates benefits in using an innovative scanning geometry in CBCT (eCT), which replaces each projection of the conventional scanning protocol with a series of collimated projections (Np) acquired over an oscillating trajectory, realized either with an oscillating source or a multi-spot array. In silico tests employed a cylindrical water phantom embodying inserts of four biological materials. 1 mm-thick bone slabs were sandwiched between 9 mm water slabs to evaluate the image conspicuity. eCT improved the Hounsfield Unit (HU) accuracy, with a direct relation with Np. eCT with Np = 10 reduced the bias of the estimated HU more than two times when compared to CBCT. Increasing the Np presented a large impact on the image conspicuity for portions of the FOV distant from the central axial plane, with the signal-to-noise ratio between water and bone slabs increasing by a factor of 18 for Np = 10 compared to CBCT. The proposed eCT configuration is expected to be adopted in applications without strict demand for scanning time and projection number, such as dentomaxillofacial and intrasurgical imaging, imaging of the extremities, and image-guided radiotherapy.

Keywords: CBCT; multi-source CBCT; quantitative imaging; innovative scanning geometry; in silico proof-of-concept

Academic Editor: Adam Konefał

Received: 15 December 2025
Revised: 22 January 2026
Accepted: 27 January 2026
Published: 29 January 2026

1. Introduction

Cone-beam Computed Tomography (CBCT) [1] is currently widely adopted in clinical applications, with use in dentomaxillo-facial and head radiology [2–4], image-guided radiotherapy treatments [5], musculoskeletal system imaging [6,7], angiography and interventional radiology [8,9] and advanced 3D breast imaging techniques [10]. In these fields, it is preferred to other similar radiological techniques—such as helical multi-detector CT scanners (MDCT)—for its high effectiveness/cost ratio, versatility, and compact size. However, it presents two intrinsic limitations that are the root-causes of image

quality degradation: (1) the large amount of scatter radiation reaching the detector and (2) the cone-shaped x-ray beam. The high level of detected scatter radiation (1) causes low frequency artifacts—such as shading or cupping artifacts [11,12]—and high-frequency noise, which can hide small details and small contrast details, such as microcalcification in CT dedicated to the breast [13]. The low-frequency artifacts can be reduced by means of image post-processing [12]. Instead, in order to reduce the high-frequency noise related to the detected scatter, reduction in the field of view (FOV) or hardware technical solutions are needed [13,14]. On the other hand, the cone-shaped beam (2), along with the conventional circular scanning geometry of the CBCT, causes signal undersampling in the axial direction with a related silent-cone in the Fourier transform of the reconstructed 3D images which outlines missing data [15]. The effect of this undersampling is image quality degradation, in particular for the portion of the FOV distant from the Source Plane (SP, i.e., the plane containing the source during the scan) [15]. This reduces the available FOV in the axial direction.

These limitations of the image quality compromise the use of CBCT in all those applications aiming at quantitative analysis of the reconstructed 3D images [12,16–27]. Indeed, the abundance of the scatter at the detector and the 3D-space undersampling make challenging the accurate evaluation of Hounsfield Units (HU) as well as the morphology of inclusions, in particular for the portion of the FOV distant from the SP. As an example of these limitations, the CBCT mounted on the gantry of a radiotherapy treatment couch, to verify the patient's alignment with respect to the original MDCT treatment planning, cannot be used to correct the treatment planning itself [22,25], due to the scatter abundance that leads to an error in HU evaluation up to 300 [19]. Similar drawbacks were also shown in applications related to the evaluation of mineral bone density [16,20,23] with inaccuracy in HU and local density evaluations, in breast cancer diagnosis [12], in the repeatability and reproducibility of radiomic features [21,26,27], in the detection of small skeletal lesions [28], in pre- and post-surgical implant evaluations [29–33], and in automatic image segmentation [34]. The reduction in the FOV is a possible strategy for decreasing both scatter and cone-artifacts in CBCT. However, the CBCT was already unfavorably reviewed by radiologists for its limited FOV in comparison to MDCT [15], and alternative strategies are needed.

An innovative approach aimed at reducing the impact of the scatter and the cone aperture artifacts has proposed the use of a multi-source scanner [15,35–40] with scanning geometries that follow trajectories different from the conventional circular scan. Hence, in these configurations, more than one source is placed along a segment parallel to the rotational axis of the scanner, either as an array of single sources [15,38] or a source with more than one focal spot [35–37]. This allows collecting projections from different distances from the conventional SP, permitting a denser sampling, in particular in the z-Fourier direction, with a related reduction in the sampling silent cone [15].

In this work, we conducted an in silico investigation of an innovative scanning geometry (eCT), which relies on an oscillating scanning trajectory and a collimated beam, to reduce the FOV undersampling and the scatter radiation, respectively. The eCT configuration substitutes each of the projections in conventional CBCT with a series of collimated projections distributed in the axial direction and acquired over an oscillating source trajectory. Such an oscillating source trajectory may be obtained either (i) via the oscillation of the conventional source in the axial direction during the rotation or (ii) via the aforementioned use of an array of x-ray sources, as previously proposed in refs [15,35–38]. The former approach is meant to reduce the costs related to the use of multi-source scanners with conventional x-ray tubes [38], and to overcome the scarce availability of multi-spot x-ray sources on the market. On the other hand, the oscillation of a conventional single spot source may induce gantry deformations and image artifacts in cases of fast scanning protocols.

https://doi.org/10.3390/app16031404

The aim of the work is to evaluate the accuracy of the HU estimates and conspicuity in eCT reconstructed images as a function of the position in the FOV. Investigations have been carried out via Monte Carlo simulations with the objective of outlining the advantages of the proposed oscillating acquisition trajectory and to parametrize the number of focal spots/projections per oscillation. In such a way, this study extends the work in refs. [35,37]—limited by the use of eight focal spots and small FOV aiming at maxillofacial imaging—and that in ref. [41]—where the image noise of eCT was characterized. Evaluations are meant to demonstrate the advantages introduced with respect to the conventional circular CBCT scanning geometry in terms of conspicuity and HU estimates, toward quantitative use of the scanner.

2. Materials and Methods

2.1. The eCT Scanning Protocol

The eCT scanning geometry substitutes each of the projections acquired in CBCT with more than one collimated projection (Np). Beam collimation in the axial direction has the objective of reducing the amount of scatter reaching the detector, with that impinging on the detector out of the primary beam being cropped during projection post-processing. This implies a reduction in the scatter-to-primary ratio (SPR) in the beam primary footprint that may reach up to 86% when 29.9 cm axial extent at the detector surface is reduced to 3.1 cm [41]. These collimated projections are acquired over an oscillating source trajectory for compensating the axial collimation as well as with the aim of reducing cone artifacts, whose main cause in CBCT is the circular orbit of the source. Figure 1 reports a schematic of the scanning geometry, where it can be observed that the projections are actually acquired just over a semi-period of the oscillation (Figure 1a). While in CBCT, the FOV includes all the portions of the reconstructed volume irradiated at least once per projection, in eCT, it includes all the volume irradiated at least once per oscillating period. The projections over the single period are acquired in such a way that they are contiguous in axial direction at the external surface of the reconstructed FOV [41]. While the gantry rotates in the axial plane, the image projections are sequentially acquired for the source position moving over an oscillating trajectory, as depicted in Figure 1a. With H being the maximum vertical distance between two source locations over an oscillating period, the y coordinate of the source position over the oscillation period yi with i going from 0 and (Np−1) can be calculated as:

$$y_i = \frac{H}{2} cos\left(\frac{\pi \cdot i}{Np - 1}\right) \quad (1)$$

In this reference system, y = 0 corresponds to the central rotating plane, i.e., SP in CBCT. As depicted in Figure 1a, the projections are acquired exclusively over one semi-period of oscillation. Since the proposed scanning geometry substitutes each of the full-field projections of the conventional CBCT with Np projections contiguous in the axial direction (Figure 1b), it does not cause undersampling of the FOV. On the other hand, there are some parts of the FOV that are irradiated twice per oscillation period (Figure 1b). In these overlapping regions, there is an increment of the FOV sampling that determines a reduction in the null-cone in the 3D Fourier domain (i.e., missing signal evident in the Fourier domain) and a reduction in the signal coefficient of variation (i.e., reduction in the high-frequency noise) [41]. As an additional benefit, the proposed geometry extends the available FOV in the axial direction, limiting the cone truncation characterizing conventional CBCT [37]. The FOV extent may be derived from geometrical consideration and the number of source locations in the axial direction [41].

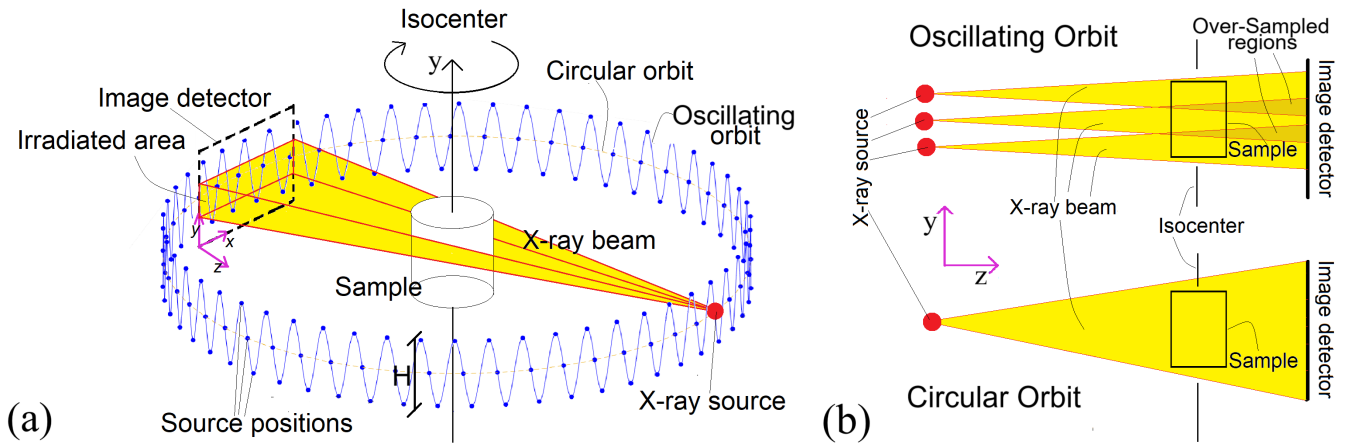

Figure 1. (**a**) eCT oscillating scanning geometry representation with a collimated beam that partially irradiates the detector. The blue dots on the oscillating path (3 per scan period in this example) represent the location of the x-ray source in which images are acquired. (**b**) Lateral view of the configuration of irradiation with 3 source locations in the axial direction (top) for collimated oscillating sources compared to a conventional full-field irradiation with CBCT (bottom). The 3 irradiations for the oscillating geometry—which replace the single one in circular orbit—were flattened in a single coronal plane for simplification.

2.2. The Digital Phantom

Studies were conducted employing the digital phantoms represented in Figure 2. It is a voxelized cylindrical water phantom with a diameter of 16.0 cm and a length of 20.0 cm, made of cubic voxels of 0.1 mm × 0.1 mm × 0.1 mm. It is placed in the eCT FOV with the cylinder axis laying on the scanner axis of rotation and the middle plane placed on the central axial plane of the FOV (i.e., SP in CBCT). The upper portion of the phantom includes cylindrical inserts with diameter of 0.8 cm and length of 1.0 cm placed at 5.0 cm from the axis of the phantom. This sets the distance between the center of the inserts and the phantom edge to 3.0 cm. The inserts were made of adipose tissue, bone, cartilage, and muscular tissue, respectively. The compositions of the considered tissues were taken from ICRP 110 [42], as made available by the simulation software (sect. 2.3) [43]. The four inserts were placed with the center at 0.5 cm from the middle plane of the phantom, as in Figure 2a. In order to study the reproducibility of the reconstructed HU over the FOV extent, the inserts were also placed with the center at 2.5 cm, 4.5 cm, 6.5 cm, and 8.5 cm from the central plane of the phantom (Figure 2b).

The lowest part of the phantom contains 0.1 cm-thick cylindrical slabs made of bone tissue with a diameter equal to that of the phantom (Figure 2b). The 9 slabs are separated by 0.9 cm of water and the first one is placed in correspondence with the middle plane of the phantom. Such slabs are meant for the evaluation of the details' conspicuity into the reconstructed image as a function of the distance from the central plane in CBCT, as performed with a Defrise phantom in ref. [15].

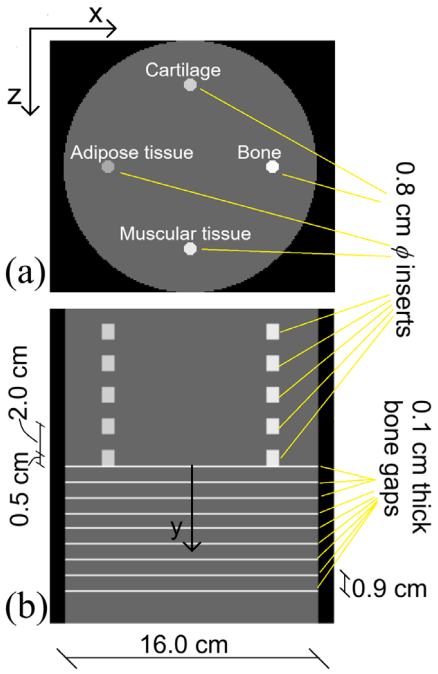

Figure 2. (**a**) Axial and (**b**) coronal views of the digital phantom used in this work. It is made of water and includes inserts of 4 different materials, namely adipose tissue, bone, cartilage, and muscular tissue, whose densities and compositions were taken from ICRP 110 [42]. The inserts were placed at 3 cm from the phantom edge at several distances from the middle plane of the phantom, which corresponded to the plane containing the source orbit in CBCT. In the lower portion of the phantoms, 0.1 cm-thick slabs made of bones are placed with a repetition period of 1.0 cm.

2.3. The In Silico Platform

The eCT acquisitions were simulated via MC-GPU v1.3, a Monte Carlo software developed at the FDA (Silver Spring, MD, USA) [43]. This software is able to simulate CBCT projections on Graphic Processor Units (GPUs). In this study, it was used by taking advantage of a NVIDIA V100 GPU reaching about 3.5×10^8 launched events per second. The software calculates the projections reporting the total energy fluence for each pixel. As output, it produces images due to primary photons separated from those obtained for the secondary (scattered) photons. In order to estimate the linear attenuation coefficient of the water for the HU calibration of the reconstruction, the 3D image of a water phantom was reconstructed from the primary projections and the attenuation coefficient estimated from a 50 × 50 voxel region in the central axial slice of the FOV. The simulations employed a 90 kV x-ray spectrum generated from a tungsten anode with an added filtration of 4 mm of Al (1st HVL = 4.16 mm Al). The simulated detector, whose efficiency was 100%, had a size of 29.9 cm × 29.9 cm with a pixel pitch of 0.146 mm. A 2 × 2 binning process over the simulated projections was used before 3D reconstructions for reaching an effective pixel size of 0.292 mm. Before the binning, the simulated projections were spatially filtered with a Gaussian filter (std dev = 2 pixels) for avoiding aliasing due to the uncorrelated noise of the ideal simulated detector and for reducing the spatial resolution toward a realistic one [44]. The beam collimation in the axial direction was changed on the basis of Np [41] in order to have a FOV extent in the axial direction (y direction) of 16.0 cm. In the case of Np = 1 and full-field irradiation of 29.9 cm × 29.9 cm at the detector surface, simulations employed 2×10^{11} primary photons per projection. With the increase of Np, the number of photons per projection was reduced in order to have a constant kerma-area product (KAP) for the oscillating period. Investigations in this work have been performed for Np = 1 (CBCT as reference), 3, 5, 7, and 10.

Three-dimensional volume reconstructions were computed via customized open software presented in a previous study [41] and available at ref. [45]. Reconstructions had a cubic voxel of 0.292 mm × 0.292 mm × 0.292 mm. In order to focus the investigation on the benefits due to the scanning geometry, no beam hardening correction and scatter reduction algorithms have been applied.

2.4. HU Accuracy Evaluation

The accuracy of the reconstructed *HU* was evaluated as the difference (ΔHU) between the actual *HU* for the insert materials and the ground truth value (HU_{GT}) as follows:

$$\Delta HU = HU - HU_{GT} \quad (2)$$

The actual *HU* value was evaluated in circular ROIs with a diameter of 20 voxels placed at the center of the considered insert. The ground truth values were evaluated from the reconstructions obtained for the primary projections, with ROIs placed within the insert close to the middle plane. ΔHU was evaluated at various distances from the middle plane. The ROIs were selected by avoiding the portions of the FOV irradiated twice per oscillation period.

2.5. Conspicuity Evaluation

The image conspicuity was evaluated as the signal-to-noise ratio (SNR) between the bone slabs and the background water phantom (Figure 2b), as follows:

$$SNR = \frac{S_{peak} - S_{bkg}}{\sigma_{bkg}}, \quad (3)$$

where S_{peak} is the peak value of the bone slab evaluated over an image profile along the axial direction, S_{bkg} is the average voxel value evaluated in a ROI placed in the water background close to the considered insert, and σ_{bkg} is the voxel standard deviation evaluated in the mentioned background ROI. The evaluations were performed in coronal slices, i.e., in slices perpendicular to the bone slabs. The ROIs were selected by avoiding the portions of the FOV irradiated twice per oscillation period.

3. Results

3.1. HU Accuracy

Figure 3 reports the ΔHUs evaluated for the four material inserts contained within the phantom. The uncertainty was estimated propagating the uncertainty on each single value, evaluated as standard deviation of the voxel values. The HU ground truth was evaluated from the 3D reconstruction obtained from the projections involving the sole primary photons. These ground truth values were estimated from the insert close to the SP to avoid influence of the cone-artifacts. Then, the accuracy was estimated as the difference between the estimated HU in a ROI contained within the insert and the ground truth values. Due to the presence of the scatter radiation, the estimated HU values are always lower than the ground truth values, determining a negative accuracy in Figure 3. The HU accuracy improves (ΔHU reduces) with increased Np. For Np = 10, the estimated HU differed from the ground truth for less than 50 in absolute value for adipose, cartilage, and muscle inserts, with the exception of cartilage inserts further from the plane. The ΔHU reached about 200 HU for the bone insert (Figure 3d). On the other hand, for Np = 1 (i.e., CBCT), such differences ranged between about −100 HU (Figure 3b) and −800 HU (Figure 3d). The HU accuracy for the cartilage inserts increased six times, moving from Np = 1 to Np = 10 at 0.5 cm from the middle plane; this ratio reduced to 2 at 6.5 cm from the middle plane. Furthermore, the aforementioned accuracy ratios resulted, respectively, in 7 and 2 for both the adipose and muscle inserts, confirming a trend with the distance from the

middle plane. Exclusively in the case of the bone insert, it remained about 4, at any considered distance from the SP. The inserts located at the extreme border of the FOV presented a relatively higher difference from the ground truth (Figure 3a–c).

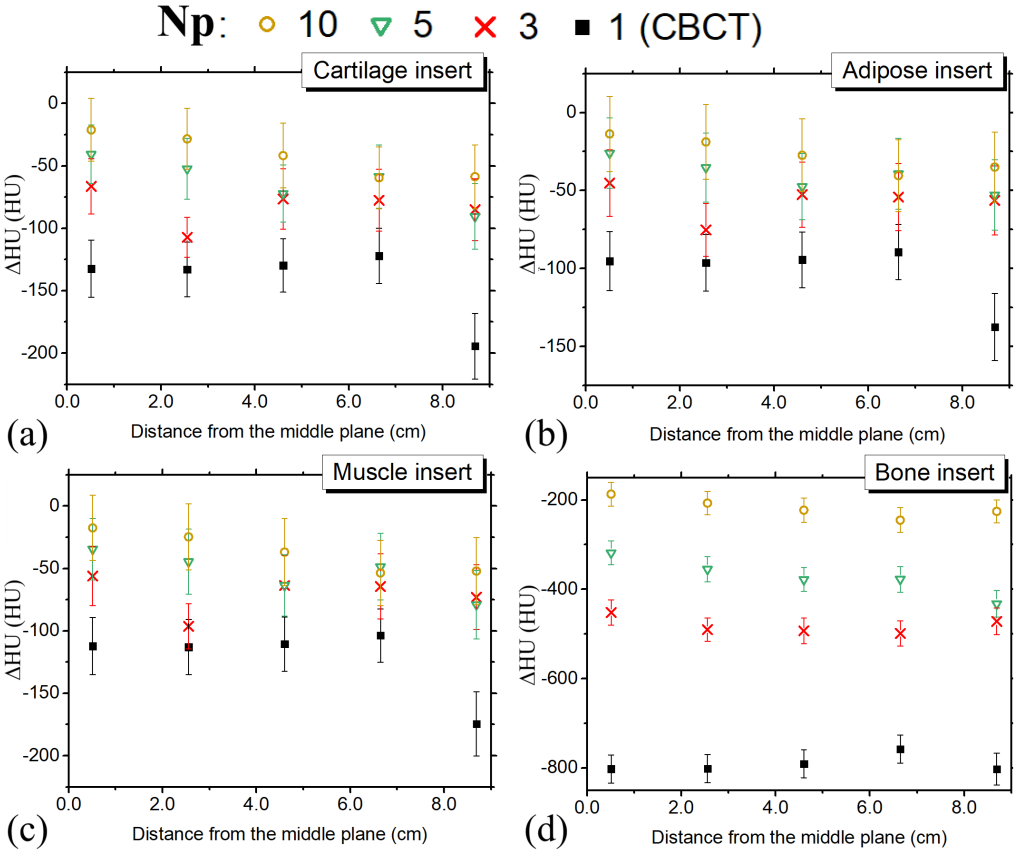

Figure 3. ΔHU as a function of the distance from the middle plane SP (i.e., the plane including the source trajectory in Np = 1). ΔHU was evaluated as the difference between HU in the reconstructed image and the HU ground truth estimated from a reconstruction obtained using the sole primary photons for the four insert materials: (**a**) cartilage, (**b**) adipose tissue, (**c**) muscle, and (**d**) bone.

3.2. Image Conspicuity

Figure 4 reports ROIs of the reconstructed coronal slices passing through the scanner rotation axis in correspondence of the lower portion of the phantom, which includes the 'Defrise-like' portions. It is noticeable that the 0.1 cm slabs of bone tissue are better delineated for the highest Np. In particular, in CBCT (Np = 1), just the slab laying in the plane containing the source orbit is well defined, even though the cupping artifact reduces its visibility at the center of the slice. When moving far from the SP, the slab conspicuity drastically reduces, appearing split in two. With the increase of Np, the number of well-defined slabs increases, with their maximum visibility corresponding to the axial source locations. Such behavior was already reported in images obtained with 6 [15] and 8 [37] source CBCT scanners, and here it is generalized. When moving at 5.0 cm from the rotation axis (Figure 5a), the conspicuity of the slabs increased for all the investigated Np, preserving the higher visibility for larger Np, in particular for portions of the reconstructed FOV far from the SP.

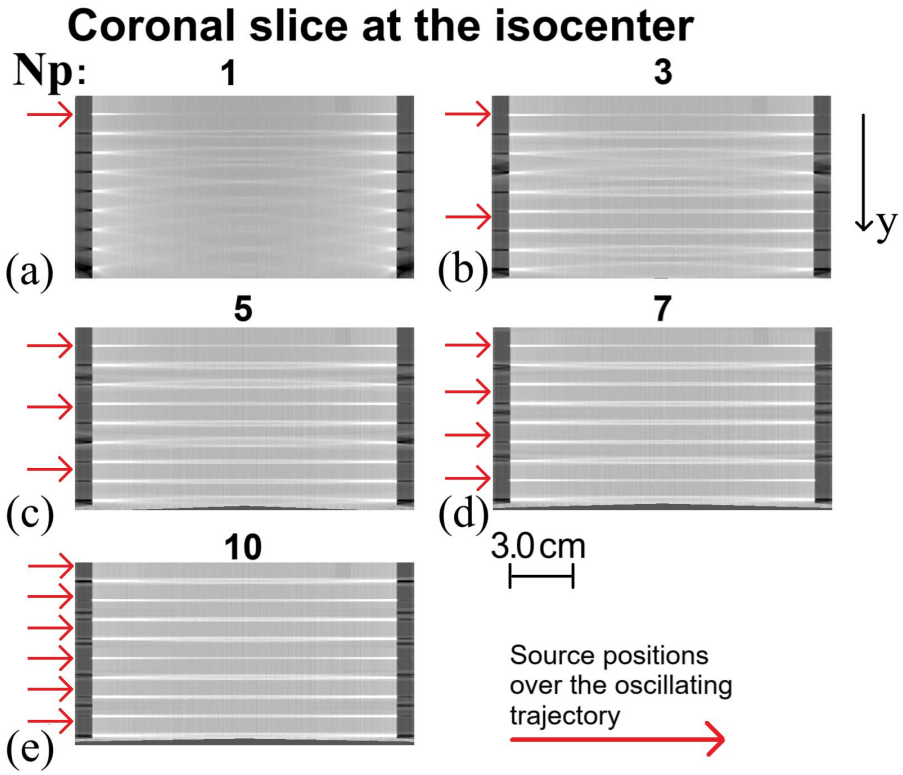

Figure 4. Coronal slices at the scanner isocenter for Np = 1 (**a**), 3 (**b**), 5 (**c**), 7 (**d**), and 10 (**e**). The selected ROIs include the lower portion of the phantom, which contains the bone slabs used for the image conspicuity evaluations. Red arrows indicate the vertical position of the source during the oscillating trajectory for the selected Np. HU windows = [−1800; 600].

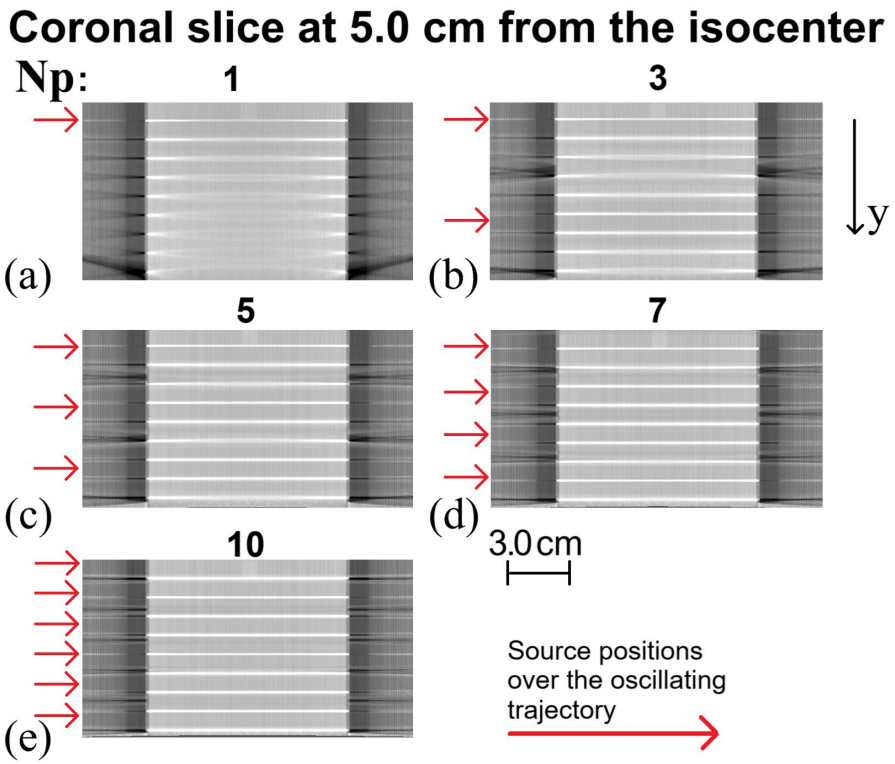

Figure 5. Coronal slices at 5.0 cm from the scanner isocenter for Np = (**a**) 1, (**b**) 3, (**c**) 5, (**d**) 7, and (**e**) 10. The selected ROIs include the lower portion of the phantom, which contains the bone slabs used for the image conspicuity evaluations. Red arrows indicate the vertical position of the source during the oscillating trajectory for the selected Np. HU windows = [−1800; 600].

https://doi.org/10.3390/app16031404

Image profiles along the rotation axis across the bone slabs are reported in Figure 6, for Np = 10, 5, and 1, respectively. It is evident that the slab conspicuity improves for a larger Np. Hence, the bone signal peak is higher for a larger Np, and the doubling effect reduces with respect to CBCT (Np = 1), in particular for portions of the FOV distant from the reconstructed middle plane. It can also be observed that the background signal is higher for a larger Np. This is due to the reduction in the scatter radiation reaching the detector, as already outlined in the discussion on the HU accuracy. Similarly, Figure 7 reports image profiles tracked on a segment parallel to that in Figure 6, at 5.0 cm from the isocenter (i.e., over the coronal slices in Figure 5). In this case, the influence of the cupping artifact is reduced and the difference in conspicuity becomes more evident, particularly at larger distances from the FOV middle plane, where the peaks of the bone slabs are drastically reduced in CBCT.

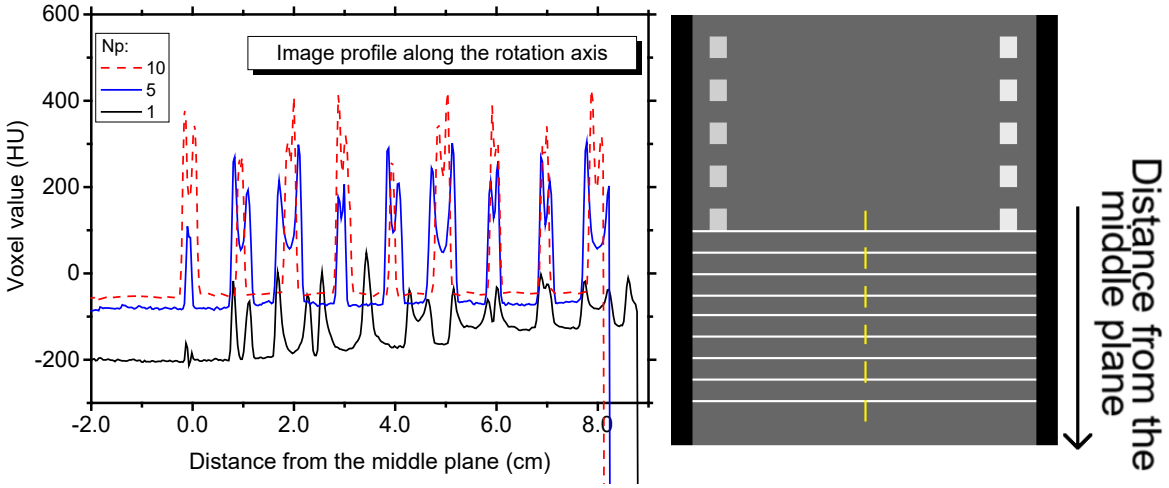

Figure 6. Image profiles along the rotation axis from coronal reconstructed images in correspondence to the bone slabs (Figure 4) and Np = 1 (CBCT), 5, and 10. On the right, the dashed line tracks the profile over the phantom.

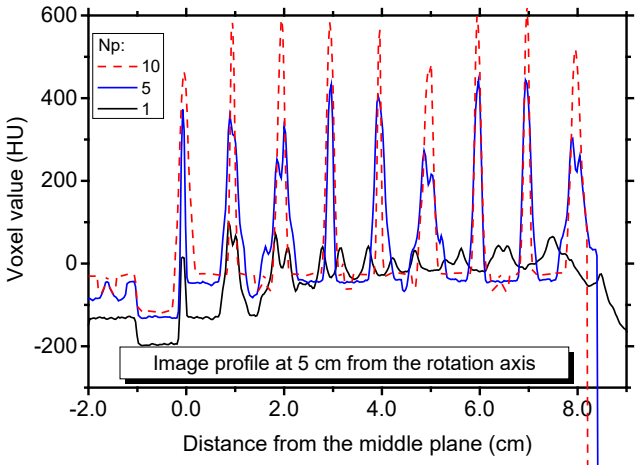

Figure 7. Image profiles in the axial direction along a segment at 5 cm from the rotation axis from coronal reconstructed images in correspondence to the bone slabs (Figure 5) and Np = 1 (CBCT), 5, and 10.

The SNR evaluated between the bone slab peaks and the water background outlines the visibility improvement due to the increase of Np (Figure 8). Along with this, it can also be noticed that, with the increase of Np, the dependence of the image conspicuity on the position also reduces. In the case of Np = 1, at 5 cm from the rotational axis, the SNR has the maximum value of 79 for the slab contained in the SP. This value reduces almost

monotonically as the distance from the middle plane increases, down to 12 at 72 mm from SP (Figure 8a). In the cases of Np = 3, it can be noticed that the SNR peaks for the slabs positioned close to the planes containing the source during the projection acquisition, reaching 217 in correspondence of the middle plane and up to 401 at 6 cm. The SNR for Np = 3 is higher or equal than that for Np = 1 for any distance from the middle plane. The maximum SNR values in correspondence of the axial positions of the sources are also evident for Np = 5, reaching the value of 371. For Np = 7 and Np = 10, the distances between consecutive source positions over the semi-period of oscillating acquisition are further reduced, and the local maxima of the SNR curve as a function of the distance from the SP are not resolved. This determines a reduced dependence between the image conspicuity and the position over the FOV. The highest SNR value is obtained for Np = 10 at 4 cm from the middle plane, where it reaches 407. It should be noted that estimated uncertainty of SNR evaluations is in the order of 12%. This is obtained as the squared sum of the background standard deviation and the standard deviation of the peak estimates over consecutive profiles.

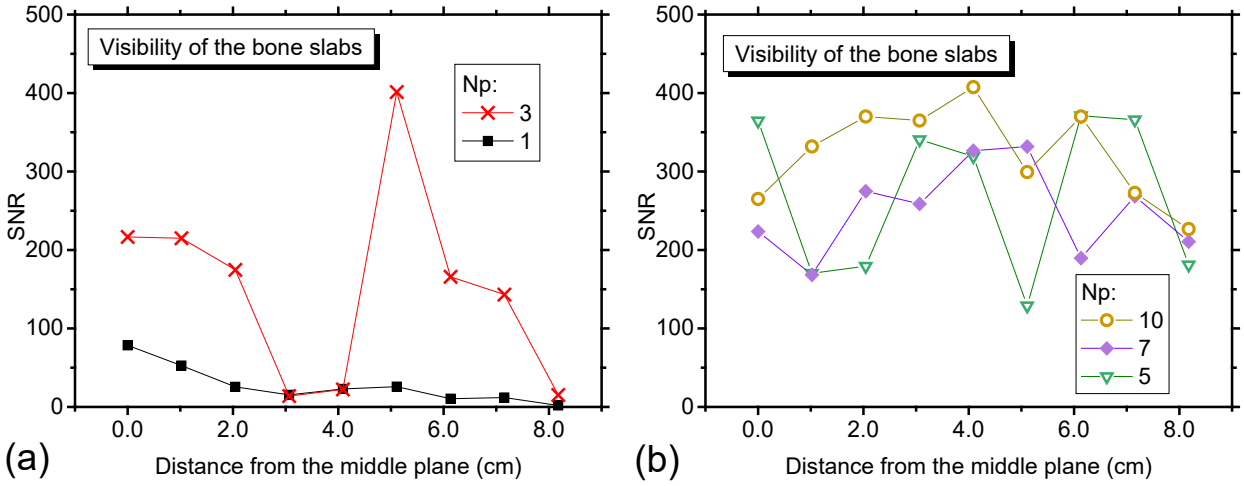

Figure 8. SNR between the water background and bone slabs from the reconstructed volume evaluated at 5.0 cm from the z axis for (**a**) Np = 1 and 3, and (**b**) Np = 5, 7, and 10.

4. Discussion

The use of an innovative configuration in CBCT, which relies on multiple-spot sources [15,35–37,46], has provided evidence of improved image quality, mainly limited by the scatter abundance and by the cone-angle artifacts in conventional configuration. The research group at the University of North Carolina at Chapel Hill (Chapel Hill, NC, USA) [35,37,39,46] investigated the use of a multi-spot source constituted of 8 focal spots interspaced by 1.2 cm, for a total extension of the source array of 8.4 cm, covering a FOV suitable for maxillofacial investigations. Such an x-ray source used cold cathodes based on carbon nanotube technology which allows embodying several focal spots in a single tube without excessive physical size. They demonstrated a considerable increase in homogeneity in the reconstructed axial slices [35], contrast-to-noise improvement up to 56% [37], and a slight improvement of the HU values which moved toward those evaluated in MDCT in an experimental phantom study [35]. Moreover, the proposed configuration demonstrated an improvement in accuracy in the evaluations of bone density with respect to conventional CBCT [46]. As also shown for three and six spots in Becker et al. [15], the denser sampling from the use of multi-spot sources increases the image conspicuity as the number of sources increases. However, Becker et al. [15] did not describe the hardware

configuration of the system, foreseeing future developments based on a multi-spot source based on conventional hot-cathode technology [47,48].

In this work, we have investigated, via in silico Monte Carlo studies, the impact that the use of an oscillating scanning trajectory—that may be obtained either via the employment of multiple spot configurations or via the use of a source oscillating in the axial direction—has on the HU estimates and on the image conspicuity. In particular, we investigated the impact of the number of sources, extending the previous literature works based on 3, 6, or 8 sources. Additionally, the use of in silico studies employing digital phantoms permitted us to set the ground truth (i.e., expected HU values), while in the experimental studies, it was taken from images acquired via multi-detector CT or nominal values [37]. This study used a reconstructed field-of-view of 16 cm in the axial direction, thereby moving beyond studies on maxillofacial imaging [35], which involved smaller detectors and FOV. While a dedicated controller in the multiple source configuration may permit generating an effective source trajectory that emulates that obtained with a single oscillating one, challenges related to the use of a single oscillating source are mainly due to the mechanical demand with the source oscillating between 130 and 500 times [1] during the scanning period that usually does not exceed 60 s. Mechanical solicitations introduced by the source oscillation can be mitigated by extending the scanning time and making the technology eligible for those applications with no strict demand for short scanning times and a large number of projections, such as imaging of the extremities, intra-surgical imaging for surgical navigation and follow-up, dento-maxillo facial imaging, and image-guided radiotherapy. On the other hand, the configuration with a single oscillating source may offer a simple solution based on conventional x-ray tubes, since the availability of multi-spot sources is still limited and their use may unjustifiably increase the cost of the apparatus.

The substitution of each projection in CBCT with several collimated projections acquired over an oscillating orbit has been shown to reduce the difference between evaluated and expected HUs, thereby improving HU accuracy. In particular, we outlined a direct relation between the number of projections per oscillation (Np) and the HU accuracy. For the cartilage, adipose, and muscular tissue inserts, the absolute differences between the HU ground truth and the measured values were always lower than 50, in the case of Np = 10. On the other hand, in CBCT (Np = 1), such a value was larger or close to 100, in absolute value. Cone artifacts presented a huge impact on the HU in CBCT for the furthest considered inserts, located at the border of the FOV.

The oscillating trajectory presented a large impact on the image conspicuity, in particular for the portion of the reconstructed FOV distant from the central axial plane. It is evident that the visibility of the details—here simulated as 0.1 cm bone slabs sandwiched between 0.9 cm water slabs—is better in correspondence with the axial locations of the source. The impact of the axial position of the source on the image conspicuity is not evident for a large Np (7 and 10), where details' visibility is constant over the axial direction. The improvement of the conspicuity of the bone slabs as a function of Np is made evident both from the reconstructed coronal slices and from the SNR analysis. In particular, from the coronal slices, it is possible to note the large number of sharp slabs in correspondence of the largest Np, whose degradation in visibility is evident by a 'doubling effect' of the slabs in coronal or sagittal slices for low Np. For Np = 10, the SNR between the slabs' signal and the water background was up to 18 times higher than for Np = 1.

Improvements in HU accuracy and in the image conspicuity over the reconstructed FOV allow for a reduction in the performance gap between CBCT and MDCT in terms of image quality and reliability of quantitative analysis. These advancements in image quality potentially make the eCT scanner eligible for a wide range of brand-new applications with scarce or impossible implication of CBCT, such as the following: quantitative imaging for radiotherapy treatment planning [19,22]; automatic radiotherapy planning [17];

detection and characterization of small skeletal lesions [28]; pre- and post-surgical evaluation in dental implants [31]; bone mineral density assessments [16,46]; intraoperative and postoperative assessments [32,33]; spectral CBCT [36,49]; automation of image segmentation [34]; and extraction of radiomic features [23,24].

The absence of experimental validation of the proposed eCT configuration represents the main limitation of this work. In fact, the mechanical stability of the oscillation source may introduce artifacts in the reconstruction images and require estimation of the actual position of the spot over the scanning trajectory. Additionally, the study is limited to investigations on a simple geometrical phantom, without focusing on specific anatomical structures or clinical indications.

5. Conclusions

We investigated, in silico, the benefits of adopting the eCT scanning configuration as advancement of the conventional CBCT scanning geometry. This innovative scanning geometry relies on an oscillating trajectory with a collimated beam, substituting each of the projections in conventional CBCT with a series of collimated projections acquired over such an oscillating orbit. The eCT demonstrated to significantly increase the HU accuracy with respect to conventional CBCT. Such an improvement was assessed to be up to seven times for the muscular tissues, with a reduction at the increasing of the distance from the middle plane. In the case of the bone insert, such a ratio was about four for any distance from the central plane of the FOV. The eCT configuration also demonstrated to reduce artifacts due to downsampling of the FOV with a corresponding increase in the image conspicuity, in particular for portions of the reconstructed images distant from the central plane of the FOV.

Author Contributions: Conceptualization, A.S., A.M., C.M.M., S.P., G.P., M.P., R.d.A. and P.C.; methodology, A.S., I.V. (Immacolata Vanore), P.M., I.V. (Ivan Veronese), A.M., S.P., G.P., M.P., R.d.A. and P.C.; software, A.S., P.M., I.V. (Imma Vanore), A.M., S.P., G.P. and P.C.; formal analysis, A.S., A.M. and P.C.; investigation, A.S., A.M. and P.C.; resources, A.S., C.M.M., S.P., M.P., R.d.A. and P.C.; data curation, A.S., P.M., I.V. (Imma Vanore), A.M. and P.C.; writing—original draft preparation, A.S., I.V. (Ivan Veronese), A.M., C.M.M., S.P., G.P., M.P., R.d.A. and P.C.; writing—review and editing, A.S., I.V. (Ivan Venorese), A.M., C.M.M., S.P., G.P., M.P., R.d.A. and P.C.; supervision, A.S. and P.C.; project administration, A.S., S.P. and P.C.; and funding acquisition, A.S., I.V. (Ivan Veronese), C.M.M., S.P., M.P., R.d.A. and P.C. All authors have read and agreed to the published version of the manuscript.

Funding: We acknowledge financial support under the National Recovery and Resilience Plan (NRRP), Mission 4, Component 2, Investment 1.1, Call for tender No. 104, published on 2 February 2022 by the Italian Ministry of University and Research (MUR), funded by the European Union—NextGenerationEU–, Project Title "Q-CT" 2022EHXL8M—CUP E53D23012420006—Grant Assignment Decree No. n. 1065, adopted on 18 July 2023 by the Italian Ministry of University and Research (MUR). Monte Carlo simulations were run on the resources of the HPC IBiSCo Cluster, funded by project code PIR01_00011 "IBISCo", PON 2014-2020.

Data Availability Statement: The original contributions presented in this study are included in the article material. Further inquiries can be directed to the corresponding author.

Conflicts of Interest: The authors declare no conflicts of interest.

References

1. Fahrig, R.; Jaffray, D.A.; Sechopoulos, I.; Webster Stayman, J. Flat-panel conebeam CT in the clinic: History and current state. *J. Med. Imaging* **2021**, *8*, 52115. https://doi.org/10.1117/1.jmi.8.5.052115.
2. Distefano, S.; Cannarozzo, M.G.; Spagnuolo, G.; Bucci, M.B.; Lo Giudice, R. The "dedicated" CBCT in dentistry. *Int. J. Environ. Res. Public Health* **2023**, *20*, 5954. https://doi.org/10.3390/ijerph20115954.
3. Polizzi, A.; Serra, S.; Leonardi, R. Use of CBCT in orthodontics: A scoping review. *J. Clin. Med.* **2024**, *13*, 6941. https://doi.org/10.3390/jcm13226941.
4. Mistretta, F.; Magnini, A.; Cinci, L.; Zanobini, P.; Pisano, M.; Barcali, E.; Bocchi, L.; Nardi, C. A systematic review and meta-analysis on the concept of bone quality in dento-maxillofacial Cone Beam Computed Tomography. *Radiol. Med.* **2025**, *130*, 1193–1206. https://doi.org/10.1007/s11547-025-02052-5.
5. Webster, M.; Podgorsak, A.; Li, F.; Zhou, Y.; Jung, H.; Yoon, J.; Lemus, O.D.; Zheng, D. New approaches in radiotherapy. *Cancers* **2025**, *17*, 1980. https://doi.org/10.3390/cancers17121980.
6. Lintz, F.; de Cesar Netto, C.; Belvedere, C.; Leardini, A.; Bernasconi, A.; The International Weight-Bearing CT Society. Recent Innovations Brought about by Weight-Bearing CT Imaging in the Foot and Ankle: A Systematic Review of the Literature. *Appl. Sci.* **2024**, *14*, 5562. https://doi.org/10.3390/app14135562.
7. Doan, M.K.; Long, J.R.; Verhey, E.; Wyse, A.; Patel, K.; Flug, J.A. Cone-Beam CT of the Extremities in Clinical Practice. *RadioGraphics* **2024**, *44*, e230143. https://doi.org/10.1148/rg.230143.
8. Barral, M.; Chevallier, O.; Cornelis, F.H. Perspectives of cone-beam computed tomography in interventional radiology: Techniques for planning, guidance, and monitoring. *Tech. Vasc. Interv. Radiol.* **2023**, *26*, 100912. https://doi.org/10.1016/j.tvir.2023.100912.
9. Chahla, B.; Ozen, M. Fluoroscopy and Cone Beam CT Guidance in Robotic Interventions. *Tech. Vasc. Interv. Radiol.* **2024**, *27*, 101007. https://doi.org/10.1016/j.tvir.2024.101007.
10. Siddall, K.; Zhang, X.; O'Connell, A. Emerging clinical applications for cone beam breast CT: Changing the breast imaging paradigm. *Curr. Breast Cancer Rep.* **2024**, *16*, 134–141. https://doi.org/10.1007/s12609-024-00535-4.
11. Siewerdsen, J.H.; Jaffray, D.A. Cone-beam computed tomography with a flat-panel imager: Magnitude and effects of X-ray scatter. *Med. Phys.* **2001**, *28*, 220–231. https://doi.org/10.1118/1.1339879.
12. Ghazi, P.; Hernandez, A.M.; Abbey, C.; Yang, K.; Boone, J.M. Shading artifact correction in breast CT using an interleaved deep learning segmentation and maximum-likelihood polynomial fitting approach. *Med. Phys.* **2019**, *46*, 3414–3430. https://doi.org/10.1002/mp.13599.
13. Ghazi, P. Reduction of scatter in breast CT yields improved microcalcification visibility. *Phys. Med. Biol.* **2020**, *65*, 235047. https://doi.org/10.1088/1361-6560/abae07.
14. Zbijewski, W.; De Jean, P.; Prakash, P.; Ding, Y.; Stayman, J.W.; Packard, N.; Senn, R.; Yang, D.; Yorkston, J.; Machado, A.; et al. A dedicated cone-beam CT system for musculoskeletal extremities imaging: Design, optimization, and initial performance characterization. *Med. Phys.* **2011**, *38*, 4700–4713. https://doi.org/10.1118/1.3611039.
15. Becker, A.E.; Hernandez, A.M.; Schwoebel, P.R.; Boone, J.M. Cone beam CT multisource configurations: Evaluating image quality, scatter, and dose using phantom imaging and Monte Carlo simulations. *Phys. Med. Biol.* **2020**, *65*, 235032. https://doi.org/10.1088/1361-6560/abc306.
16. Kim, D.G. Can Dental Cone Beam Computed Tomography Assess Bone Mineral Density? *J. Bone Metab.* **2014**, *21*, 117. https://doi.org/10.11005/jbm.2014.21.2.117.
17. Amit, G.; Purdie, T.G. Automated planning of breast radiotherapy using cone beam CT imaging. *Med. Phys.* **2015**, *42*, 770–779. https://doi.org/10.1118/1.4905111.
18. Delgadillo, R.; Spieler, B.O.; Ford, J.C.; Kwon, D.; Yang, F.; Studenski, M.; Padgett, K.R.; Abramowitz, M.C.; Pra, A.D.; Stoyanova, R.; et al. Repeatability of CBCT radiomic features and their correlation with CT radiomic features for prostate cancer. *Med. Phys.* **2021**, *48*, 2386–2399. https://doi.org/10.1002/mp.14787.
19. Liang, X.; Jiang, Y.; Xie, Y.; Niu, T. Quantitative Cone-Beam CT Imaging in Radiotherapy: Parallel Computation and Comprehensive Evaluation on the TrueBeam System. *IEEE Access* **2019**, *7*, 66226–66233. https://doi.org/10.1109/ACCESS.2019.2902168.
20. Cassetta, M.; Stefanelli, L.V.; Pacifici, A.; Pacifici, L.; Barbato, E. How accurate is CBCT in measuring bone density? A comparative CBCT-CT in vitro study. *Clin. Implant Dent. Relat. Res.* **2014**, *16*, 471–478. https://doi.org/10.1111/cid.12027.
21. Yong, T.H.; Yang, S.; Lee, S.J.; Park, C.; Kim, J.-E.; Huh, K.-H.; Lee, S.-S.; Heo, M.-S.; Yi, W.-J. QCBCT-NET for direct measurement of bone mineral density from quantitative cone-beam CT: A human skull phantom study. *Sci. Rep.* **2021**, *11*, 15083. https://doi.org/10.1038/s41598-021-94359-2.

22. Mason, J.H. Quantitative Cone-Beam Computed Tomography Reconstruction for Radiotherapy Planning. Ph.D. Thesis, The University of Edinburgh, Edinburgh, UK, 2018. Available online: http://hdl.handle.net/1842/33193 (accessed on 20 January 2026).
23. Spuhler, K.D.; Teruel, J.R.; Galavis, P.E. Assessing the reproducibility of CBCT-derived radiomics features using a novel three-dimensional printed phantom. *Med. Phys.* **2021**, *48*, 4326–4333. https://doi.org/10.1002/mp.15043.
24. Fave, X.; MacKin, D.; Yang, J.; Zhang, J.; Fried, D.; Balter, P.; Followill, D.; Gomez, D.; Jones, A.K.; Stingo, F.; et al. Can radiomics features be reproducibly measured from CBCT images for patients with non-small cell lung cancer? *Med. Phys.* **2015**, *42*, 6784–6797. https://doi.org/10.1118/1.4934826.
25. Kamburoğlu, K.; Acar, B.; Yüksel, S.; Paksoy, C.S. CBCT quantitative evaluation of mandibular lingual concavities in dental implant patients. *Surg. Radiol. Anat.* **2015**, *37*, 1209–1215. https://doi.org/10.1007/s00276-015-1493-9.
26. Rossi, M.; Bruno, G.; De Stefani, A.; Perri, A.; Gracco, A. Quantitative CBCT evaluation of maxillary and mandibular cortical bone thickness and density variability for orthodontic miniplate placement. *Int. Orthod.* **2017**, *15*, 610–624. https://doi.org/10.1016/j.ortho.2017.09.003.
27. Niu, T.; Al-Basheer, A.; Zhu, L. Quantitative Cone-Beam CT Imaging in Radiation Therapy Using Planning CT as a Prior: First Patient Studies. *Med. Phys.* **2012**, *39*, 1991–2000. https://doi.org/10.1118/1.3693050.
28. Demehri, S.; Muhit, A.; Zbijewski, W.; Stayman, J.W.; Yorkston, J.; Packard, N.; Senn, R.; Yang, D.; Foos, D.; Thawait, G.K.; et al. Assessment of image quality in soft tissue and bone visualization tasks for a dedicated extremity cone-beam CT system. *Eur. Radiol.* **2015**, *25*, 1742–1751. https://doi.org/10.1007/s00330-014-3546-6.
29. Liljeholm, R.; Kadesjö, N.; Benchimol, D.; Hellén-Halme, K.; Shi, X.Q. Cone-beam computed tomography with ultralow dose protocols for pre-implant radiographic assessment: An in vitro study. *Eur. J. Oral Implantol.* **2017**, *10*, 351–359.
30. Özalp, Ö.; Tezerişener, H.A.; Kocabalkan, B.; Büyükkaplan, U.Ş.; Özarslan, M.M.; Kaya, G.Ş.; Altay, M.A.; Sindel, A. Comparing the precision of panoramic radiography and cone-beam computed tomography in avoiding anatomical structures critical to dental implant surgery: A retrospective study. *Imaging Sci. Dent.* **2018**, *48*, 269–275. https://doi.org/10.5624/isd.2018.48.4.269.
31. Suttapreyasri, S.; Suapear, P.; Leepong, N. The accuracy of cone-beam computed tomography for evaluating bone density and cortical bone thickness at the implant site: Micro-computed tomography and histologic analysis. *J. Craniofacial Surg.* **2018**, *29*, 2026–2031. https://doi.org/10.1097/SCS.0000000000004672.
32. Sheth, N.M.; De Silva, T.; Uneri, A.; Ketcha, M.; Han, R.; Vijayan, R.; Osgood, G.M.; Siewerdsen, J.H. A mobile isocentric C-arm for intraoperative cone-beam CT: Technical assessment of dose and 3D imaging performance. *Med. Phys.* **2020**, *47*, 958–974. https://doi.org/10.1002/mp.13983.
33. Vetter, S.Y.; Euler, J.; Beisemann, N.; Swartman, B.; Keil, H.; Grützner, P.A.; Franke, J. Validation of radiological reduction criteria with intraoperative cone beam CT in unstable syndesmotic injuries. *Eur. J. Trauma Emerg. Surg.* **2021**, *47*, 897–903. https://doi.org/10.1007/s00068-020-01299-z.
34. Alam, S.R.; Li, T.; Zhang, P.; Zhang, S.Y.; Nadeem, S. Generalizable cone beam CT esophagus segmentation using physics-based data augmentation. *Phys. Med. Biol.* **2021**, *66*, 65008. https://doi.org/10.1088/1361-6560/abe2eb.
35. Xu, S.; Li, B.; Inscoe, C.R.; Bastawros, D.; A Tyndall, D.; Lee, Y.Z.; Lu, J.; Zhou, O. Evaluation of the feasibility of a multisource CBCT for maxillofacial imaging. *Phys. Med. Biol.* **2023**, *68*, 175012. https://doi.org/10.1088/1361-6560/acea17.
36. Li, B.; Spronk, D.; Luo, Y.; Puett, C.; Inscoe, C.R.; Tyndall, D.A.; Lee, Y.Z.; Lu, J.; Zhou, O. Feasibility of dual-energy CBCT by spectral filtration of a dual-focus CNT X-ray source. *PLoS ONE* **2022**, *17*, e0262713. https://doi.org/10.1371/journal.pone.0262713.
37. Xu, S.; Hu, T.; Li, B.; Inscoe, C.R.; Tyndall, D.A.; Lee, Y.Z.; Lu, J.; Zhou, O. Volumetric computed tomography with carbon nanotube X-ray source array for improved image quality and accuracy. *Commun. Eng.* **2023**, *2*, 71. https://doi.org/10.1038/s44172-023-00123-x.
38. Gang, G.J.; Zbijewski, W.; Mahesh, M.; Thawait, G.; Packard, N.; Yorkston, J.; Demehri, S.; Siewerdsen, J.H. Image quality and dose for a multisource cone-beam CT extremity scanner. *Med. Phys.* **2018**, *45*, 144–155. https://doi.org/10.1002/mp.12659.
39. Xu, S.; Hu, Y.; Li, B.; Inscoe, C.R.; Tyndall, D.A.; Lee, Y.Z.; Lu, J.; Zhou, O. Multisource cone beam computed tomography using a carbon nanotube X-ray source array. In *Medical Imaging 2024: Physics of Medical Imaging*; SPIE: Bellingham, WA, USA, 2024; Volume 12925, pp. 641–649.
40. Gong, H.; Yan, H.; Jia, X.; Li, B.; Wang, G.; Cao, G. X-ray scatter correction for multi-source interior computed tomography. *Med. Phys*. **2017**, *44*, 71–83.
41. Minopoli, A.; Pardi, S.; Paternò, G.; Pugliese, M.; Cardarelli, P.; Sarno, A. Noise power properties of a cone-beam CT scanner with unconventional scanning geometry. *Phys. Med.* **2025**, *130*, 104888. https://doi.org/10.1016/j.ejmp.2024.104888.
42. ICRP. ICRP Publication 110: Adult Reference Computational Phantoms. *Ann. ICRP* **2009**, *39*. Available online: https://www.icrp.org/publication.asp?id=icrp%20publication%20110 (accessed online on 20 January 2026)

43. Badal, A.; Badano, A. Accelerating Monte Carlo simulations of photon transport in a voxelized geometry using a massively parallel graphics processing unit. *Med. Phys.* **2009**, *36*, 4878–4880. https://doi.org/10.1118/1.3231824.
44. Sarno, A.; Tucciariello, R.M.; Fantacci, M.E.; Traino, A.C.; Valero, C.; Stasi, M. A model for a linear a-Se detector in simulated X-ray breast imaging with Monte Carlo software. *IEEE Trans. Radiat. Plasma Med. Sci.* **2024**, *8*, 263–268. https://doi.org/10.1109/TRPMS.2024.3349563.
45. Minopoli, A.; Sarno, A. CBCT/ExoCT Reconstruction Software. Available Under Creative Common Attribution 4.0 License. 2024. Available online: https://www.openaccessrepository.it/records/wxdh6-2y475 (accessed on 20 January 2026).
46. Hu, Y.; Xu, S.; Li, B.; Inscoe, C.R.; Tyndall, D.A.; Lee, Y.Z.; Lu, J.; Zhou, O. Improving the accuracy of bone mineral density using a multisource CBCT. *Sci. Rep.* **2024**, *14*, 3887. https://doi.org/10.1038/s41598-024-54529-4.
47. Boone, J.M.; Becker, A.E.; Hernandez, A.M.; Dobbins, J.T.; Schwoebelc, P. Multi-X-ray source array for stationary tomosynthesis or multi-cone angle cone beam CT. In *Medical Imaging 2019: Physics of Medical Imaging*; Bosmans, H., Chen, G.-H., Gilat Schmidt, T., Eds.; SPIE: Bellingham, WA, USA, 2019; Volume 10948. https://doi.org/10.1117/12.2512959.
48. Sisniega, A.; Hernandez, A.M.; Shakeri, S.A.; Morris, E.A.; Boone, J.M.; Siewerdsen, J.H.; Schwoebel, P.R. A multiple X-ray-source array (MXA) system with a planar two-dimensional source distribution for digital breast tomosynthesis. *Med. Phys*. **2024**, *51*, 8709–8724. https://doi.org/10.1002/mp.17452.
49. Hu, Y.; Li, B.; Xu, S.; Inscoe, C.R.; Tyndall, D.A.; Lee, Y.Z.; Lu, J.; Zhou, O. A Dual-Energy CBCT With Reduced Scatter and Cone Beam Artifacts Using an X-Ray Source Array and Interlaced Spectral Filters. *IEEE Trans. Biomed. Eng*. **2026**. https://doi.org/10.1109/TBME.2026.3651411.